JOURNAL OF THERMOPHYSICS AND HEAT TRANSFER
Vol. 6, No. 3, July–Sept. 1992

Turbulent Transport Phenomena in a Channel with Periodic Rib Turbulators

T.-M. Liou,* J.-J. Hwang,† and S.-H. Chen‡
National Tsing Hua University, Hsinchu, Taiwan 30043, Republic of China

Periodic fully developed turbulent flow in a two-dimensional channel with rib turbulators on two opposite walls has been studied numerically and experimentally. In numerical predictions, an algebraic Reynolds stress turbulence model is adopted, and a smoothed hybrid central/skew upstream difference scheme is developed. In experiments, the laser-Doppler velocimetry and laser holographic interferometry are employed to measure the local flow and heat transfer characteristics. The results are obtained with the ratio of pitch to rib height 5, 10, 15, and 20, for Reynolds number of 3.3 × 10^4 and are presented in terms of the reattachment length, mean velocity and turbulent kinetic energy profiles, isotherm patterns, and distributions of local pressure recovery and Nusselt number. A detailed comparison with experimental data shows that the present calculations have an improvement over the previous work in the prediction of periodic ribbed-wall flow and heat transfer. In addition, regions susceptible to hot spots are identified by examining the distributions of the local Nusselt number. Furthermore, the enhancement of mean Nusselt number is documented in terms of relative contributions of the increased turbulence intensity and surface area provided by the ribs.

Nomenclature

A = half width of channel
B = half height of channel
C_f = pressure drop coefficient, $2(P - P_{REF})/(\rho U_0^2)$
c_p = specific heat at constant pressure
De = hydraulic diameter
H = rib height
k = turbulent kinetic energy
k_f = air conductivity
$\underline{Nu}$ = local Nusselt number
$\overline{Nu}$ = average Nusselt number
P = pressure
Pi = rib pitch
PR = rib-pitch-to-rib-height ratio, P/H
Pr = Prandtl number
Q'' = heat transfer per unit span
$\dot{q}_w$ = local wall heat flux
Re = Reynolds number, $U \cdot De/\nu$
T = temperature of air
T_0 = local bulk mean temperature of air
T_w = local wall temperature
U = axial mean velocity
u = streamwise fluctuation velocity
v = transverse fluctuation velocity
W = rib width
X = axial coordinate
Y = transverse coordinate
Z = spanwise coordinate
β = overall pressure gradient
γ = axial gradient of T_w
ε = dissipation rate of turbulence kinetic energy
$\hat{\Theta}$ = dimensionless temperature, $(T_w - T)\rho \cdot c_p \cdot \sqrt{(\tau_w/\rho)} \cdot /\dot{q}_w$
μ = molecular dynamic viscosity
μ_t = turbulent dynamic viscosity
ρ = air density
$\sigma_T, \sigma_k, \sigma_\varepsilon$ = turbulent Prandtl number of T, k, and ε, respectively

Subscripts
i,j,k = coordinate indices
s = smooth channel
w = wall
0 = bulk mean

Received May 20, 1991; revision received Aug. 16, 1991; accepted for publication Aug. 19, 1991.
*Professor, Power Mechanical Engineering Department.
†Ph.D. Candidate, Power Mechanical Engineering Department.
‡Graduate Student, Power Mechanical Engineering Department.

Introduction

A COMMON method used for the enhancement of heat transfer in channels is to place bluff bodies on the wall of the channel to disrupt the channel flow. For instance, in gas turbine blade cooling design, repeated rib-turbulators are cast on two opposite walls of the internal cooling passages of nearly rectangular cross sections in order to enhance the removal of heat from the blade external surfaces which are directly exposed to the flow of hot gases. Moreover, to improve the thermal efficiency and power density, the trend in modern aeroengine design is toward high gas outlet temperature from the combustor; the heat transfer augmentation of turbine cooling channels becomes, therefore, more and more critical. In spite of the increase in the heat transfer rate of the ribbed channels, there exists possible "hot spots" in the cavity and corner recirculation zones where fluids are nearly stagnant relative to the core flow and local heat transfer is very poor. The local heat transfer over ribbed surface is strongly connected with the mechanism of turbulent flow characteristics. However, the technical literatures containing information on both the local turbulent flowfield and temperature field of channels with repeated ribs mounted on two opposite walls are relatively sparse.

For the sake of brevity, only the most relevant work will be cited below. Webb et al.[1] presented heat transfer and pressure drop data for the turbulent fully developed flow in circular tubes with internal transverse ribs of square profile shape, for a wide range of Prandtl numbers. The geometrical parameters were varied in ranges $0.01 \le H/De \le 0.04$ and $10 \le Pi/H \le 40$. Han[2] and Han et al.[3] systematically investigated the effects of the rib pitch-to-height ratio (Pi/H), the rib-height-to-equivalent-diameter ratio (H/De) and the rib angle of attack (α) on the heat transfer coefficient and the friction factor in the fully developed turbulent air flow in a rectangular duct which had two opposite ribbed walls. The temperature distributions in all the aforementioned work were measured by thermocouples.

For methods to simulate the turbulent flow around a body or in a straight pipe/parallel channel, Boussinesq model,

standard k-ε model (referred to as k-ε-E model in this study, E stands for eddy viscosity) and large eddy simulation (LES) have been proposed. k-ε-E model is rather popular at present and the validity of the model has been examined for several types of flow. Drain and Martin[4] predicted the turbulent flow in a ribbed-wall channel by using the k-ε-E model. They concluded the agreement between computations and laser-Doppler velocimetry (LDV) measurements for turbulence intensity and Reynolds stresses was rather poor. The reattachment length was seriously underestimated about 26%. Kobayashi et al.[5,6] performed numerical results for the turbulent flow in two-dimensional channel with turbulence promoters by using LES and the k-ε-E model, respectively. After assessment by hot-wire data, they found that LES has a greater availability than the k-ε-E model in predicting the turbulent flow investigated. Fodemski[7] presented a simulation of flow and heat transfer with standard k-ε model in channels with ribbed surface; however, there was no experimental data of flowfield patterns for comparison with their numerical predictions. It should be noted that in all the above computational studies the ribs were mounted on one wall of the channel and the spacing between the consecutive ribs was fixed.

In light of above brief survey, a systematical computational and experimental study of turbulent fluid flow and heat transfer in a rectangular channel with two opposite ribbed walls is evidently necessary. The turbulence model adopted in the present study is the algebraic Reynolds stress model (k-ε-A) which has not been previously applied to such a periodic problem. This model can be considered as an extended and improved k-ε turbulence model and appears attractive for accounting for effects of buoyancy, rotation, and streamline curvature in an economical fashion.[8] The concepts and formulation previously used in solving periodic fully developed laminar flow and heat transfer[9] will be extended to the turbulent case in the present work. Experimentally, the flowfield and heat transfer are measured by LDV and laser holographic interferometry (LHI), respectively. The comparison of the computed results of turbulent flow and heat transfer with those measured by LDV and LHI will enable an assessment of the turbulence models. In addition, another emphasis is placed on the effects of the spacing between successive rib pairs on the turbulent flow pattern, pressure recovery, isotherm pattern, and heat transfer augmentation. Information relevant to the regions susceptible to hot spots is also highly desired for the design of turbine blades and, therefore, will be investigated.

Computational Procedure

For the typical computational module shown in Fig. 1, the fluid properties of two-dimensional, incompressible, steady-state, periodic fully developed turbulent flow to be analyzed will be regarded as constant.

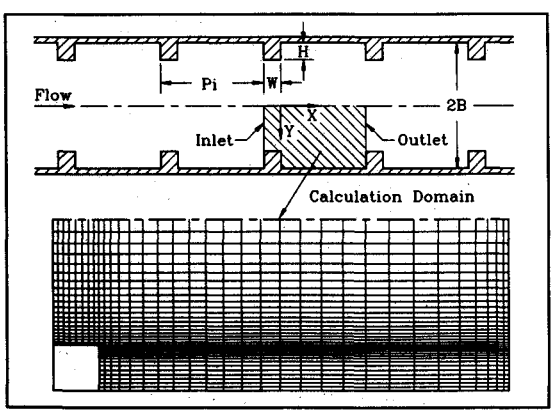

Fig. 1 Sketch of configuration and coordinate system of the test section.

Governing Equations

The Reynolds-averaged equations for conservation of mass, momentum, and energy can be written as

$$\frac{\partial(\rho U)}{\partial X} + \frac{\partial(\rho V)}{\partial Y} = 0 \tag{1}$$

$$\frac{\partial(\rho UU)}{\partial X} + \frac{\partial(\rho VU)}{\partial Y} = \frac{\partial}{\partial X}\left(\mu\frac{\partial U}{\partial X}\right) + \frac{\partial}{\partial Y}\left(\mu\frac{\partial U}{\partial Y}\right) + \beta - \frac{\partial \hat{P}}{\partial X} + \frac{\partial}{\partial X}\left(\mu\frac{\partial U}{\partial X}\right) + \frac{\partial}{\partial Y}\left(\mu\frac{\partial V}{\partial X}\right) - \frac{\partial}{\partial X}(\rho\overline{uu}) - \frac{\partial}{\partial Y}(\rho\overline{uv}) \tag{2}$$

$$\frac{\partial(\rho UV)}{\partial X} + \frac{\partial(\rho VV)}{\partial Y} = \frac{\partial}{\partial X}\left(\mu\frac{\partial V}{\partial X}\right) + \frac{\partial}{\partial Y}\left(\mu\frac{\partial V}{\partial Y}\right) - \frac{\partial \hat{P}}{\partial Y} + \frac{\partial}{\partial X}\left(\mu\frac{\partial U}{\partial Y}\right) + \frac{\partial}{\partial Y}\left(\mu\frac{\partial V}{\partial Y}\right) - \frac{\partial}{\partial X}(\rho\overline{uv}) - \frac{\partial}{\partial Y}(\rho\overline{vv}) \tag{3}$$

$$\frac{\partial(\rho c_p U\hat{T})}{\partial X} + \frac{\partial(\rho c_p V\hat{T})}{\partial Y} = \frac{\partial}{\partial X}\left(c_p\frac{\mu}{Pr}\frac{\partial \hat{T}}{\partial X}\right) + \frac{\partial}{\partial Y}\left(c_p\frac{\mu}{Pr}\frac{\partial \hat{T}}{\partial Y}\right) - \frac{\partial}{\partial X}(\rho c_p\overline{u\theta}) - \frac{\partial}{\partial Y}\cdot(\rho c_p\overline{v\theta}) - \rho c_p U\gamma \tag{4}$$

Because of the periodic behavior of the flow, the pressure and temperature, as pointed out in Rowley and Patankar,[9] can be expressed as

$$P(X,Y) = -\beta X + \hat{P}(X,Y) \text{ and } T(X,Y) = \gamma X + \hat{T}(X,Y)$$

where the pressure drop parameter $\beta = [P(X,Y) - P(X + Pi,Y)]/Pi$ and the temperature increase parameter $\gamma = [T(X + Pi,Y) - T(X,Y)]/Pi$ are constants. The term $-\beta X$ is related to the global mass flow rate $\dot{m}$ (or Reynolds number) and represents the general decrease in pressure in the axial direction, whereas the γX accounts for the fluid enthalpy rise along the axial direction. In a numerical computation, the value of β is obtained first from the experimental data and then is adjusted iteratively until the desired flow rate (or Reynolds number) is obtained. For the case of heating, it can be shown that $\gamma = Q''/(\dot{m}\cdot c_p\cdot Pi)$ in which Q'' is the rate of heating addition (per unit span) to the fluid in the period length Pi and is also given by the experiment. The functions $\hat{P}(X,Y)$ and $\hat{T}(X,Y)$ identically repeat themselves from pitch to pitch and indicate the local departure of pressure and temperature from the linear decay given by $-\beta X$ and linear increase given by γX, respectively.

The turbulence correlation stands for the Reynolds stresses and Reynolds heat fluxes that must be modeled to close the governing equations. The full Reynolds stress and Reynolds heat flux models under Rodi's assumptions[10] that the transport of $\overline{u_iu_j}$ and $u_i\theta$ is proportional to the transport of k and that proportionality factors are $\overline{u_iu_j}/k$ and $u_i\theta/2k$, respectively, can be simplified to algebraic relationships between the stresses, heat fluxes, k, ε, and derivatives of mean flow quantities

$$\frac{\overline{u_iu_j}}{k}(P_k - \varepsilon) = P_{ij} - \frac{2}{3}\delta_{ij}\varepsilon - C_{A1}\frac{\varepsilon}{k}\left(\overline{u_iu_j} - \frac{2}{3}\delta_{ij}k\right) - C_{A2}\left(P_{ij} - \frac{2}{3}\delta_{ij}P_k\right) \tag{5}$$

$$\frac{\overline{u_i\theta}}{2k}(P_k - \varepsilon) = -\left(\overline{u_iu_m}\frac{\partial T}{\partial X_m} + \overline{u_m\theta}\frac{\partial U_i}{\partial X_m}\right) - C_{T1}\frac{\varepsilon}{k}\overline{u_i\theta} + C_{T2}\,\overline{u_m\theta}\frac{\partial U_i}{\partial X_m} \tag{6}$$

which can be further reduced to

$$\frac{\overline{u_iu_j}}{k} = \frac{2}{3}\delta_{ij} + \frac{(1 - C_{A2})\left(\frac{P_{ij}}{\varepsilon} - \frac{2}{3}\delta_{ij}\frac{P_k}{\varepsilon}\right)}{C_{A1} + \frac{P_k}{\varepsilon} - 1} \tag{7}$$

$$-\frac{\overline{u_i\theta}}{k} = \frac{\overline{u_iu_m}\frac{\partial T}{\partial X_m} + (1 - C_{T2})\left(\overline{u_m\theta}\frac{\partial U_i}{\partial X_m}\right)}{\varepsilon\left[C_{T1} + \frac{1}{2}\left(\frac{P_k}{\varepsilon} - 1\right)\right]} \tag{8}$$

where $P_k = -\overline{u_mu_n}(\partial U_m/\partial X_n)$ and $P_{ij} = -[\overline{u_iu_m}(\partial U_j/\partial X_m) + \overline{u_ju_m}(\partial U_i/\partial X_m)]$.

Furthermore, the local effect of a rigid solid wall on pressure strain correlation and pressure temperature gradient correlation can be expressed through the modification of constants C_{A1}, C_{A2} and C_{T1} with the following relationships,[11,12] respectively:

$$\tilde{C}_{A1} = C_{A1} - 0.125\frac{k^{3/2}}{\varepsilon z_p} \tag{9}$$

$$\tilde{C}_{A2} = C_{A2} - 0.015\frac{k^{3/2}}{\varepsilon z_p} \tag{10}$$

$$\tilde{C}_{T1} = C_{T1} + 0.5\delta_{pi}\frac{k^{3/2}}{\varepsilon z_p} \tag{11}$$

where z_p is the distance to the solid wall and p denotes the direction normal to the wall.

The turbulent kinetic energy k and its dissipation rate ε appeared in the above equations can be obtained by solving the k equation and ε equation, which are put in the following way:

$$\frac{\partial(\rho Uk)}{\partial X} + \frac{\partial(\rho Vk)}{\partial Y} = \frac{\partial}{\partial X}\left[\left(\mu + \frac{\mu_t}{\sigma_k}\right)\frac{\partial k}{\partial X}\right] + \frac{\partial}{\partial Y}\left[\left(\mu + \frac{\mu_t}{\sigma_k}\right)\frac{\partial k}{\partial Y}\right] - \rho\overline{u_iu_j}\frac{\partial U_i}{\partial X_j} - \rho\varepsilon \tag{12}$$

$$\frac{\partial(\rho U\varepsilon)}{\partial X} + \frac{\partial(\rho V\varepsilon)}{\partial Y} = \frac{\partial}{\partial X}\left[\left(\mu + \frac{\mu_t}{\sigma_\varepsilon}\right)\frac{\partial \varepsilon}{\partial X}\right] + \frac{\partial}{\partial Y}\cdot\left[\left(\mu + \frac{\mu_t}{\sigma_\varepsilon}\right)\frac{\partial \varepsilon}{\partial Y}\right] - C_1\frac{\varepsilon}{k}\rho\overline{u_iu_j}\frac{\partial U_i}{\partial X_j} - C_2\rho\frac{\varepsilon^2}{k} \tag{13}$$

where $\mu_t = c_\mu\rho k^2/\varepsilon$ is the turbulent viscosity and the associated empirical constants are given in Table 1.[13] Note that for the k-ε-A calculations, the use of the eddy viscosity in Eqs. (12) and (13) is restricted to the diffusion term alone. Although, to be consistent, $\partial/\partial X_i[(k/\varepsilon)\overline{u_iu_j}(\partial k/\partial X_j)]$ and $\partial/\partial X_i[(k/\varepsilon)\overline{u_iu_j}(\partial\varepsilon/\partial X_j)]$ should be used for the diffusion terms in the k-ε-A model, the forms $\partial/\partial X_j[(\mu + \mu_t/\sigma_k)\partial k/\partial X_j]$ and $\partial/\partial X_j[(\mu + \mu_t/\sigma_\varepsilon)\partial\varepsilon/\partial X_j]$ in Eqs. (12) and (13) are found to yield higher computational stability, and they are therefore used here throughout. Similar treatment has also been found in Ref. 14.

Table 1 Constants in k-ε-A model

C_1	C_2	σ_k	σ_ε	C_{A1}	C_{A2}	C_{T1}	C_{T2}	C_μ
1.44	1.92	1.0	1.3	2.3	0.4	3.2	0.5	0.09

Boundary Conditions

The above set of partial differential equations has to be solved with the following boundary conditions:

1) Symmetric plane ($Y = 0$)

$$\frac{\partial U}{\partial Y} = \frac{\partial k}{\partial Y} = \frac{\partial \varepsilon}{\partial Y} = \frac{\partial \hat{P}}{\partial Y} = \frac{\partial \hat{T}}{\partial Y} = 0,\ V = 0$$

2) Periodic conditions at the upstream and downstream ends of the computational domain (Fig. 1)

$$U(X,Y) = U(X + Pi,Y),\quad V(X,Y) = V(X + Pi,Y)$$
$$k(X,Y) = k(X + Pi,Y),\quad \varepsilon(X,Y) = \varepsilon(X + Pi,Y)$$
$$\hat{T}(X,Y) = \hat{T}(X + Pi,Y),\quad \hat{P}(X,Y) = \hat{P}(X + Pi,Y)$$

3) Channel walls and rib surfaces

In this study, the near-wall region was simulated by two zone model, i.e., viscous sublayer and fully turbulent zone, and the wall-function method[15] was used to bridge the viscous sublayer. The wall function approach consists of the assumption that at the grid points nearest to the solid wall, that is, at a distance y_p from the nearest wall, a component parallel to the wall (U_p) obeys the following equation:

$$U_p/\sqrt{(\tau_w/\rho)} = \rho\cdot y_p\cdot\sqrt{(\tau_w/\rho)}/\mu \quad \rho\cdot y_p\sqrt{(\tau_w/\rho)}/\mu \le 11.6$$
$$U_p/\sqrt{(\tau_w/\rho)} = \frac{1}{\kappa}\ln[\rho\cdot E\cdot y_p\cdot\sqrt{(\tau_w/\rho)}/\mu] \quad \rho\cdot y_p\cdot\sqrt{(\tau_w/\rho)}/\mu > 11.6 (E = 9.79) \tag{14}$$

and the assumption that at the same location the production of k is in equilibrium with the dissipation of k. If k_p and ε_p are the k and ε at $Y = y_p$, then it can be shown that the conditions imposed on the k equation and ε equation instead of solid-wall boundary conditions are

$$k_p = (\tau_w/\rho)/\sqrt{C_\mu} \quad \text{and} \quad \varepsilon_p = (\tau_w/\rho)^{3/2}/(\kappa y_p) \tag{15}$$

In addition, for a given constant wall heat flux $\dot{q}_w$ the time-averaged mean temperature at point p is obtained from

$$(\hat{T}_w - \hat{T}_p + \gamma\cdot\Delta x)\cdot\rho\cdot c_p\cdot\sqrt{(\tau_w/\rho)}/\dot{q}_w = \sigma_T[\rho\cdot y_p\cdot\sqrt{(\tau_w/\rho)}/\mu],\quad \rho\cdot y_p\cdot\sqrt{(\tau_w/\rho)}/\mu \le 11.6$$
$$\cdot(\hat{T}_w - \hat{T}_p + \gamma\cdot\Delta x)\cdot\rho\cdot c_p\cdot\sqrt{(\tau_w/\rho)}/\dot{q}_w = \sigma_T\left\{\frac{1}{\kappa}\cdot\ln[\rho\cdot E\cdot y_p\cdot\sqrt{(\tau_w/\rho)}/\mu] + 9.24 \cdot[(Pr/\sigma_T)^{3/4} - 1]\cdot[1 + 0.28\cdot\exp[-0.07(Pr/\sigma_T)]]\right\},\quad \rho\cdot y_p\cdot\sqrt{(\tau_w/\rho)}/\mu > 11.6 \tag{16}$$

where $\Delta x = x_w - x_p$. The second term on the right-hand side of the lower Eq. (16) is the P-function which was deduced directly from experimental data by Jayatilleka.[16]

Solution Method

A finite difference scheme CSUDS (Hybrid Central/Skew Upstream Difference Scheme) was proposed by Leschziner[17]

to reduce numerical diffusion associated with one-dimensional discretization schemes (e.g., power law difference scheme and hybrid difference scheme) as large cross-flow gradients existed and the flow cut across the grid lines at a large angle.[18] However, Leschziner's CSUDS led to a discontinuity occurring as the Peclet number (Pe) equaled two and, in turn, led to numerical oscillation during iteration. To improve the aforementioned disadvantage in CSUDS, the upwind difference scheme, instead of the central difference scheme adopted in CSUDS, was employed to discretize the diffusion term, as $|Pe| > 2$. The reason is that as $|Pe| > 2$ the convection dominates over the diffusion and the prediction by the upwind difference scheme is generally better than by the central difference scheme.[19] Also note that the increase of false diffusion by the upwind scheme is negligible, since the upwind scheme is applied to diffusion term only. After the above modification, the discretization results show no discontinuity occurring as $|Pe| = 2$ and the iteration running rather smoothly. The improved CSUDS will be referred to as SCSUDS (smoothed hybrid central/skew upstream difference scheme) in the present study. As for handling the pressure-velocity coupling arising in the implicitly discretized fluid flow equations, the method PISO (pressure implicit with splitting of operators)[20] was utilized in this paper for the reason of stable and faster convergence.[21] The convergence problem encountered in the present work was handled with a dual-loop method. The mean flow, mean temperature, and turbulence model variables (k and ε) were solved in an outer loop by using the CTDMA (cyclic tridiagonal-matrix algorithm) line-by-line iteration with small under-relaxation factors for the numerical stability, whereas the Reynolds stress and Reynolds heat flux were computed explicitly from Eqs. (7) and (8) in an inner loop which utilizes Gauss-Seidel point iteration with under-relaxation. The tolerance of the overall sum of nondimensionalized residual was typically 0.005.

A nonuniform grid arrangement was used in the present computations and shown in Fig. 1. The grid system was staggered with velocity nodes displaced from scalar nodes. Grid independence test was performed with four different grid sizes, namely 20 × 20, 30 × 30, 36 × 36, and 52 × 52. The parameters used to check the grid independence of the computational results were the reattachment length, which has historically been used to assess the overall predictive capability of turbulence models, and turbulent kinetic energy profiles. The deviations in the reattachment length from the grid size of 52 × 52 were found to be 10.6%, 3.5%, and 1.1% respectively, for grid sizes of 20 × 20, 30 × 30, and 36 × 36. A comparison of calculated turbulent kinetic energy profiles among using 20 × 20, 36 × 36, and 52 × 52 grids was further made in Fig. 2 where the two axial stations of $X/H = -0.5$ and $X/H = 3.0$ were selected since they crossed the rib top and separation bubble. The differences of k/U_0^2 between two succeeding grids shown in Fig. 2 became small, confirming that the results were converging towards the grid-independence solution. Consequently, the grid size 36 × 36 was chosen in the present work. The corresponding CPU time on a CDC-CYBER 180/840 computer is about 4.5 s for each iteration, and it typically needs 2000 to 3000 iterations to reach convergence.

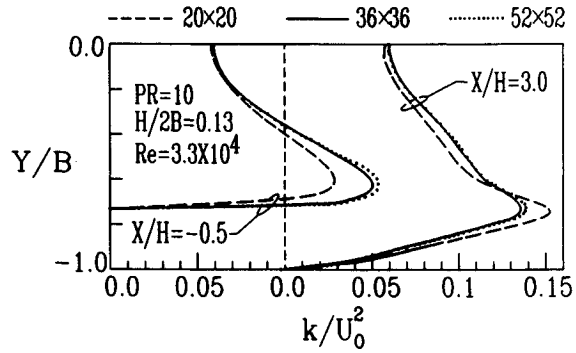

Fig. 2 Grid dependence of calculated turbulent kinetic energy.

Experimental Program

Experimental Apparatus

The flow system is shown in schematic form in Fig. 3. Air at room temperature was drawn into the test section through a flow straightener and four screens in the settling chamber and a 10:1 contraction by a 3 hp blower at the downstream end. The air then flowed through the test section, a flow straightener, a rotameter and a bellows; and was then exhausted by the blower.

Measurements of mean velocities and turbulent kinetic energy were obtained with a laser Doppler velocimeter described in detail in Liou and Kao.[22] The holographic interferometer used for temperature-field measurements is shown schematically in Fig. 3. Coherent light (514.5-nm wavelength) from a 3-W argon-ion laser was split into an object beam and a reference beam by a variable-silvered mirror, and each beam was then expanded to a 150-mm planar wave by a telescope and a collimating lens. The telescope consists of a 40× microscope objective and a 10-μm-diam pinhole. The pinhole was located at the focal point of the microscope objective in order to eliminate intensity variations in the wave front. The object wave passed through the test section, where the temperature field was to be examined, whereas the reference wave directly fell onto the photographic plate. The plate was held in the liquid gate to provide in-place development of plate, as required for real time work. The photographic emulsion 8E56, made by Agfa-Gevaert Limited, was found to be a suitable recording material for the present work. Through a CCD camera, the instantaneous interference field was monitored on a multisync monitor and recorded on a VHS videocassette recorder for storage and further image processing.

Two test channels were used in the present study. One was a heat transfer test channel and the other was a pressure drop test channel. The heat transfer test channel was 1200 mm in length and had a rectangular cross section 160 × 40 mm² (YZ-plane). Square ribs (brass) of size 5.2 × 5.2 mm² were glued periodically in-line on the upper and lower heated plates (aluminum) of the test channel. Each heated plate was well insulated with fiberglass and balsa wood. The construction of

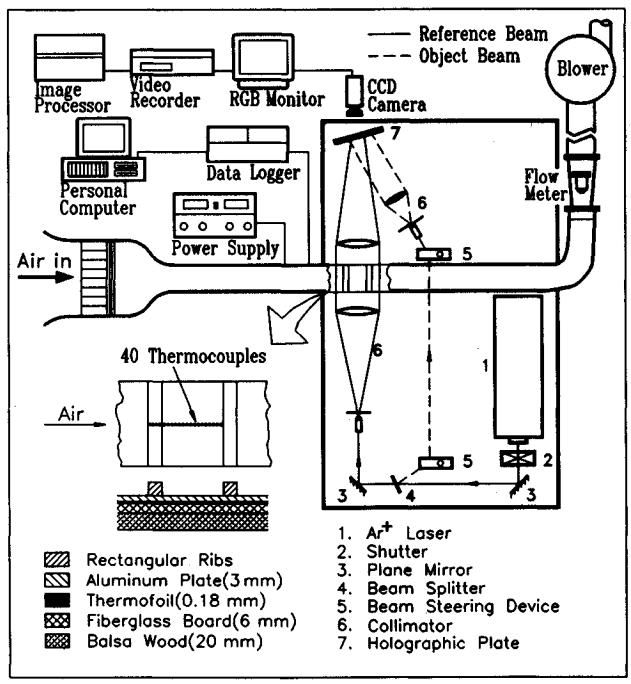

Fig. 3 Schematic drawing of overall experimental system and construction of heated plate.

the two walls were displayed in detail in Fig. 3. The side walls of the entire heated test channel were made of plexiglass plates to provide optical access for LDV and LHI measurements. For wall temperature measurements, 40 copper-constantan thermocouples were installed in the heated plates and ribs, as shown in Fig. 3. The junction-beads of 0.25-mm diam were cemented into small holes drilled into the back side of the heated plates and ribs, approximately 1.0 mm from the wetted surfaces. A Yokogawa DA-2500 hybrid recorder and a PC-AT were used for temperature readings and recordings.

The internal geometry of the pressure drop test channel was similar to that of the heat transfer test channel. The only difference was Plexiglas (adiabatic) instead of aluminum (heated) for construction. A Pitot tube of 0.8-mm diameter was inserted from the upper ribbed plate to transverse across and along the flow direction to allow static pressure measurements of air flow. The pressure drop of the present study was based on the adiabatic conditions (without heating), as what has been done in Han et al.,[3] and was measured by a Kyowa PDL-40B microdifferential transducer with an accuracy up to 0.1%. The measured pressure signal was subsequently amplified by a Kyowa WGA-200A amplifier and read from a digital readout.

Periodic Fully Developed Condition

For the purpose of comparing with the present predictions of the periodic fully developed flows, the measurements were made in the region between the 19th and 20th ribs ($15.4 \leq X/De \leq 16.2$) from the channel inlet. According to the results obtained by Sparrow and Tao[23] and Han et al.,[3] the local Nusselt number distributions between the ribs became uniformly cyclic after about 3–5 hydraulic diameters from the duct inlet. In addition, the work of Chang[24] reported that both mean-velocity and turbulent intensity profiles attained periodic fully developed condition after 480 mm ($X/De \cong 10$) in the rectangular-rib roughened duct. These facts implied that both thermally and hydrodynamically periodic fully developed conditions were achieved in the region investigated.

Data Reduction and Uncertainty

In this study a holographic interferometer was employed to reveal the entire temperature field, and subsequently enable the calculations of local and mean Nusselt numbers along the heated surface.[25] Before initiating the LHI work, a two-dimensionality check on the spanwise temperature profiles of the air flow was conducted by using the thermocouple probes. As shown in Fig. 4, the scatter of the temperature in the spanwise direction was less than 6% of the channel spanwise average temperature. The local Nusselt number was calculated from the local temperature gradient at wall, the local wall temperature, and the local bulk mean temperature as

$$Nu = De \cdot (dT/dY)_w/(T_w - T_0) \qquad (17)$$

where $(dT/dY)_w$ was obtained by using a second-order, least-square curve fit to the temperature field measured by LHI. The local bulk mean temperature, T_0, was calculated from an energy balance. And the local wall temperature, T_w, was read from the thermocouple output. The errors in estimating the temperature gradient along the heated walls are within 3%. And the maximum uncertainty in estimating the Nu is of the order of 6.5% according to the uncertainty estimation method of Kline and McClintock.[26]

The distributions of the local pressure drop in the channel were normalized by the fluid dynamic pressure as

$$C_f = (P_x - P_{REF})/[(\tfrac{1}{2})\rho U_0^2] \qquad (18)$$

where P_{REF} is the reference pressure. The maximum uncertainty in the local pressure drop was estimated to be less than 7.1%.

As for the LDV measurements, representative values of uncertainty estimates are noted in figure captions. More detailed uncertainty estimates are included in Liou and Kao.[22]

Results and Discussion

Reattachment Length

The calculated characteristic lengths of the recirculation zones on the trailing (X_R) and leading (X_S) sides of the rib for test range of PR are displayed in Fig. 5. The measured results in the present work for $PR = 10$ and by Hijikata et al.[27] for $PR = 15$ are included for comparison. It is seen from this plot that the computed and measured results are in reasonably good agreement. For the case of $PR = 10$, the reattachment and separation on the channel wall can be clearly found. As PR is further increased, the lengths of both recirculation zones alter slightly, typically $X_R = (3.7 \pm 0.3)H$ and $X_S = (0.60 \pm 0.06)H$, respectively. Hence, for large PR

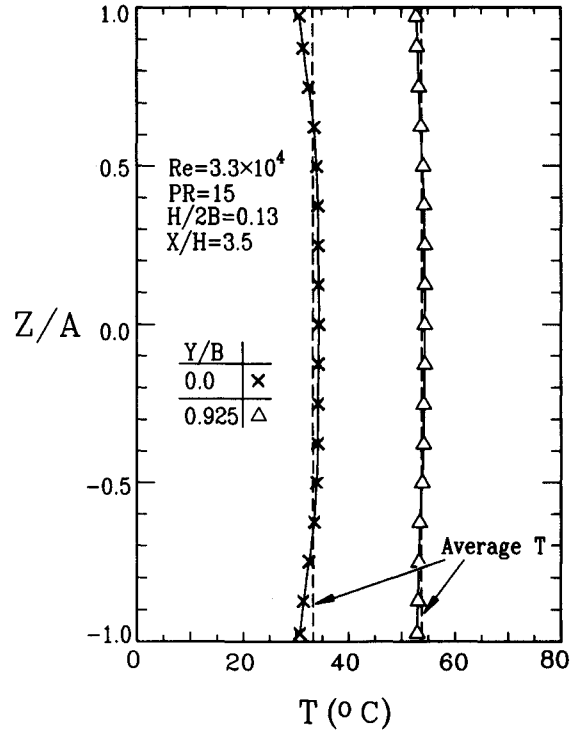

Fig. 4 Temperature profiles along the channel spanwise direction.

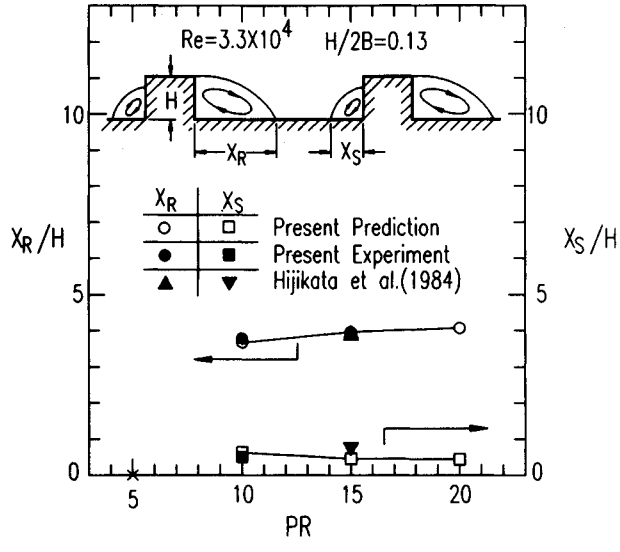

Fig. 5 Calculated (k-ε-A model) and measured characteristic length of the recirculation zone for $PR = 10$, 15, and 20 with $W/H = 1.0$, $H/2B = 0.13$, and $Re = 3.3 \times 10^4$.

values, the two recirculation zones occupy a smaller portion of the channel wall. It is noted that the heat transfer from the channel wall is obviously influenced by the presence of the recirculation zones and reattachment,[22] as this will be shown later. For $PR = 5$, both flow separation and reattachment do not take place on the channel wall but on the ribs to form a cavity flow. The recirculation zone in the cavity prevents the fluid near the central plane from a direct contact with the cavity wall and hence has a great influence on the heat transfer characteristics, and this will also be demonstrated later.

Mean Velocity and Turbulent Kinetic Energy

The measured (LDV) and computed (k-ε-A) streamwise mean velocity and turbulent kinetic energy profiles at selected axial stations which cut across the rib top ($X/H = -0.5$), the recirculation zone ($X/H = 3.5$), and the redeveloping zone ($X/H = 7.0$) along $Z/A = 0$ plane are shown in Fig. 6 for $PR = 10$. In this plot, the k-ε-E prediction[24] is also included for comparison. In general, the agreement between the computed and measured results is satisfactory. The streamwise mean velocity profiles shown in Fig. 5 display that the k-ε-A model predicts a better flow reversal in the separation bubble ($X/H = 3.5$) than the k-ε-E model. The reattachment lengths (X_R) computed by the k-ε-A and k-ε-E models and measured by LDV are $(3.7 \pm 0.3)H$, $(3.2 \pm 0.3)H$, and $(3.8 \pm 0.4)H$, respectively; the corresponding discrepancies between the calculated and measured values are within 2.6% and 15.8%, respectively. It is to be noticed that the comparison made above reveals that even the k-ε-A model underpredicts the velocity recovery behind the rib pair of the order of $0.2\ U_0$ and the maximum velocity of the order of $0.05\ U_0$. A survey of related calculations using k-ε-E and higher-order turbulence models in separated and reattaching flows[17,28,29] also indicates similar underpredictions from the order of 0.5–1.0 U_0. One of the reasons for the underprediction of separated flow region is that the near-wall treatment of all the aforementioned calculations using different turbulence models is based on the wall law which is only valid for the normal boundary layers.

The widely used approximation[30] of turbulent kinetic energy $k = \frac{3}{4}(u^2 + v^2)$ is employed in this work. It is shown in Fig. 6 that the value of k is lower in the core-flow region, as expected for periodic fully developed turbulent flows. On the other hand, large value of k is found in the shear layers and in the flow-separation regions where high velocity gradient exists. The discrepancy between the calculated and measured k lies mainly in the shear layers and near-wall regions. In general, the k-ε-A model predicts a better result in turbulent kinetic energy than the k-ε-E model, especially near the rib top where an improvement up to 30% of measured value is found. This is because the k-ε-A model accounts for the significant anisotropy along the shear layers and near the walls, but the k-ε-E model does not.

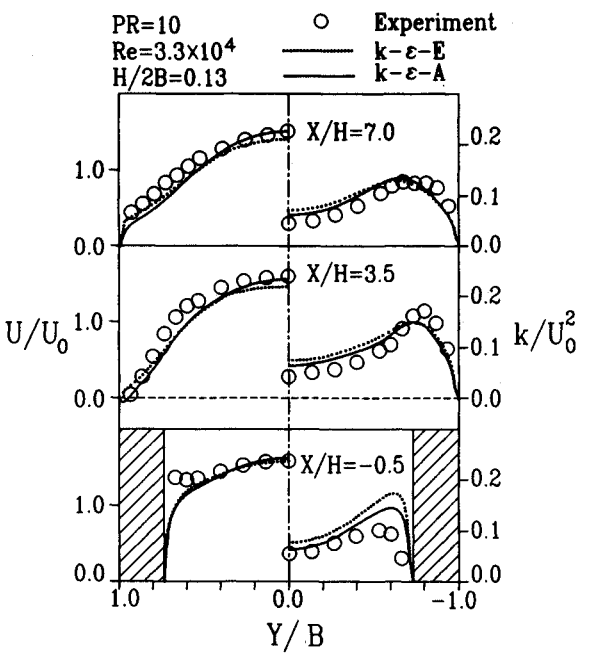

Fig. 6 Streamwise mean-velocity and turbulent kinetic energy profiles at axial stations of $X/H = -0.5$, 3.5, and 7.0 along plane $Z/A = 0$ for $PR = 10$ (Experimental uncertainty in U/U_0: less than ±3.2%; in $k^{1/2}/U_0$: less than ±10%.)

Local Pressure Drop

Figure 7 displays the computed and measured streamwise distributions of the dimensionless pressure drop along the centerline of the ribbed channel for $PR = 5$, 10, 15, and 20. The smooth channel results (dash-dotted line) are included for comparison. Basically, the variation of centerline pressure is correlated with that of periodic mean velocity field. For $PR = 5$, the periodic distribution of the dimensionless local pressure drop is almost as a straight line but slightly convex in the region at a short distance upstream of each rib, where the corresponding dividing streamline is slightly concave at the same region. For $PR = 10$, due to the flow reattachment and separation on the channel wall between the successive ribs, the dividing stream lines associated with the channel walls behave like a divergent-convergent nozzle, and the corresponding centerline pressure accordingly increases and decreases, as shown in Fig. 7. As PR is further increased, the patterns of local pressure distribution between two successive ribs are similar but stretched along streamwise direction. It is worthwhile to note that the large pressure loss caused by the existence of rib pairs is clearly revealed by the discrepancy of C_f between ribbed channel flow and smooth channel flow investigated by the present work. As shown in Fig. 7, the k-ε-A model provides a better agreement with the measured C_f data than the k-ε-E model since the k-ε-A model predicts a centerline mean velocity more closer to the measured one (Fig. 6).

Isotherm Pattern

The computed isotherms, based on the k-ε-A turbulence model, for $PR = 5$, 10, 15, and 20 are shown in Fig. 8. For $PR = 5$, the temperature distribution between two consec-

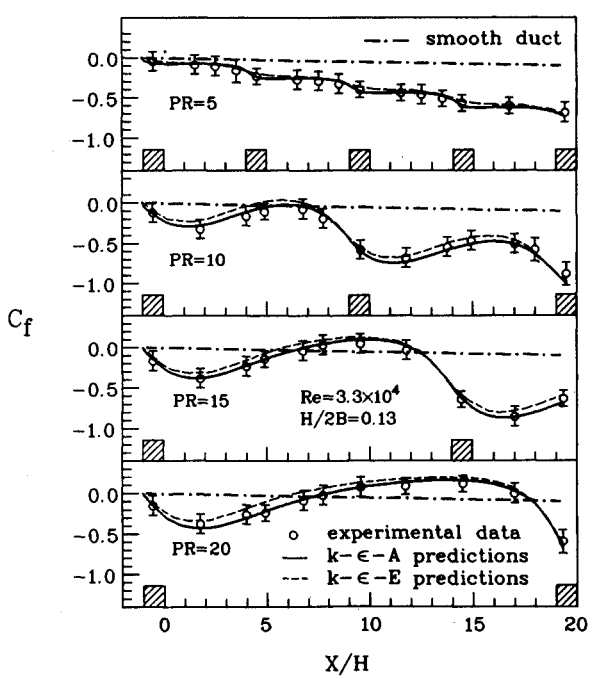

Fig. 7 Streamwise distributions of dimensionless static pressure along the centerline for $PR = 5$, 10, 15, and 20 with $H/2B = 0.13$ and $Re = 3.3 \times 10^4$.

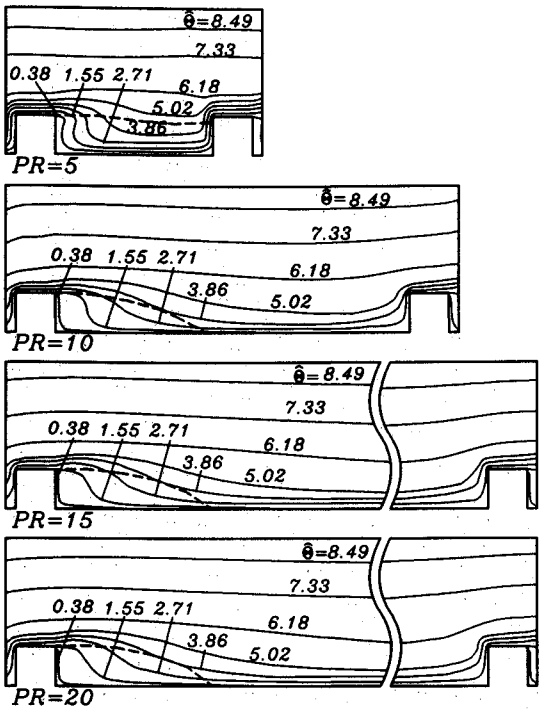

Fig. 8 Calculated isotherms (k-ε-A model) for PR = 5, 10, 15, and 20 with $H/2B$ = 0.13 and Re = 3.3 × 10^4.

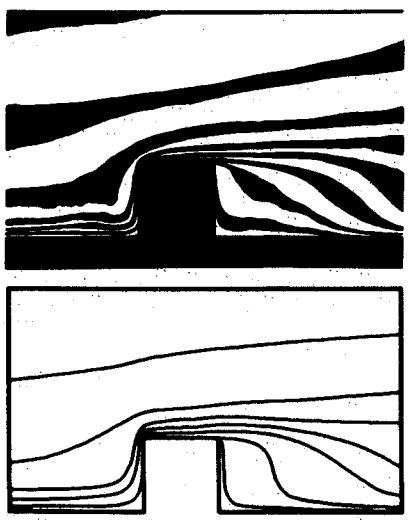

Fig. 9 Comparison of calculated (k-ε-A model) and measured (LHI) isotherms for PR = 15 with $H/2B$ = 0.13 and Re = 3.3 × 10^4.

utive ribs is similar to that in flow over a cavity. The isotherms are roughly perpendicular to the dividing streamline (dashed line), especially for the region near the front side of each rib. This fact implies that dividing streamline acts like an adiabatic wall to prevent heat transfer from passing through it. As $PR \geq 10$, the temperature of fluid in the core region is altered slightly, and the significance of thermal diffusion is confined to the recirculating regions around the rib; therefore, arc-shaped isotherms which are similar to those in a cavity flow happened here. In addition, the redeveloping (secondary) thermal boundary layer is found downstream of reattachment point and near the rib top. It is noteworthy that the nondimensional isotherms $\hat{\Theta}$ (a function of $\hat{T}$) displayed in Fig. 8 are identical cyclically from pitch to pitch.

In order to compare with the isotherms measured by LHI, the predicted temperature $\hat{T}$ must be transferred into T which increases linearly from pitch to pitch along the flow direction. A comparison of the measured and the predicted isotherms near the ribbed heated wall is shown in Fig. 9. Both these results are obtained for the periodic fully developed flows. The pattern of isotherms that measured by LHI is in reasonably good agreement with numerical results. The discrepancy between the two results is within 9%. It can be seen from Fig. 9 that the fringes in the near rib-top region become thinner and get closer to each other. This implies a region of high heat transfer rate. On the other hand, the arc-shaped fringes near the center of recirculation behind rib become thicker and the spacings between fringes are wider. And both these imply a region of stagnant fluid and low heat transfer rate. This will be demonstrated later.

Local Heat Transfer

The local Nusselt number ratio, calculated from the k-ε-A model and measured by using LHI for the case of PR = 15, Re = 3.3 × 10^4, and $H/2B$ = 0.13, is plotted as a function of position along the wetted surface for two consecutive ribs in Fig. 10. The results predicted by the k-ε-E model are included in Fig. 10 for comparison. It is obvious from the plot that both the k-ε-A model and the k-ε-E model predictions are in good agreement with measured results in the portion of inter-rib space; however, in the rib top region, the k-ε-E model performs a much worse agreement with measured data than the k-ε-A model. This is reasonable because poor prediction of turbulent kinetic energy by k-ε-E model employing with isotropic assumption is obtained from flowfield in this portion as mentioned above.

It is known that the heat transfer augments in ribbed channel not only by the extra surface area added by ribs but also by the increase of turbulence. Figure 10 further illustrates the close correlation between the local Nusselt number ratio and turbulent kinetic energy distribution. Both $Nu/\overline{Nu}_s$ and k show the presence of the local maximum on the top of rib and at the place slightly upstream of reattachment point. The former is due to enhanced force convection of flow acceleration and turbulent transport by sudden contraction. The latter is due to impingement of reattaching flow on the channel wall. Additionally, both calculated and measured results reveal that the two concave corners formed by the intersection of the

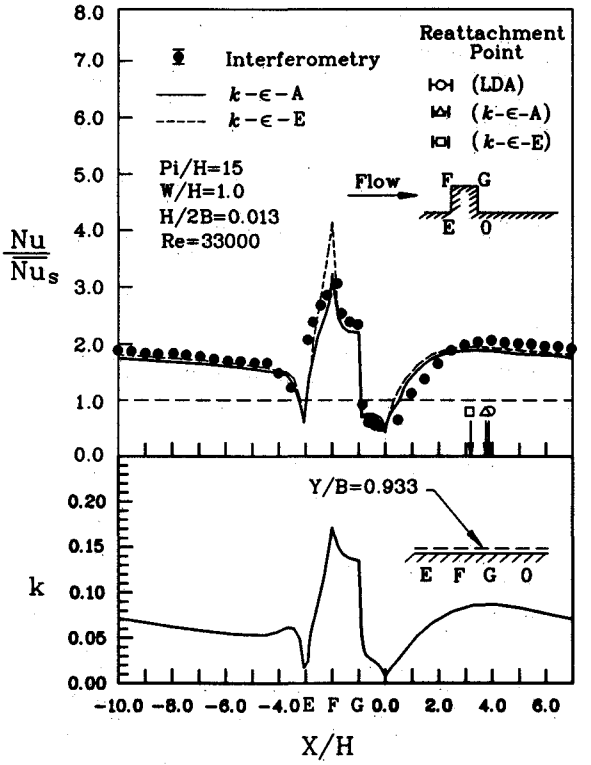

Fig. 10 Streamwise distributions of calculated and measured local Nusselt number ratio and calculated turbulence kinetic energy for PR = 15.

rib and channel wall ($-1.0 < X/H \leq E$ and $G \leq X/H \leq 1.0$) are susceptible to hot spots since poor heat transfer occurs in these regions.

The calculated results based on the k-ε-A model to illustrate the effect of rib spacing on the local heat transfer coefficients are shown in Fig. 11. For $PR = 5$, the distribution of local Nusselt number ratios exhibits a local peak along the heated wall. The local peak is located at a little distance downstream of middle point of the heated wall because of strong convection induced by the core flow. It is worthwhile to note that Chen and Yoon,[31] by using finite analytic numerical method, come to the same conclusion in their study of laminar cavity flow for $Re = 2000$. Additionally, heat transfer is particularly strong on the EF and FG surfaces, and local Nusselt number ratios remain to be minimum at both concave corners (E,G) of the rib. For $PR \geq 10$, as shown in Fig. 11, the distribution of local Nusselt number ratios from regions upstream of reattachment alters slightly within one-pitch range; however, downstream of reattachment point, the local Nusselt number ratio has larger distance for continuous decay as PR increased. This is because of wider rib spacing, creating thicker boundary-layer thickness after flow reattachment between ribs.

Mean Heat Transfer

One of the main objectives of this study is to determine the influence of the ribs on the heat transfer from the channel wall to the fluids. For this purpose, a mean Nusselt number in one pitch is defined by $\overline{Nu} = Q''De/[Pi(\bar{T}_w - \bar{T}_0)k_f]$. In order to place the results on a common basis, $\overline{Nu}$ is based on the projected area of a corresponding ribless channel, rather than on the actual surface area (including the extra area provided by the presence of the ribs) of the ribbed channel. Thus, the magnitude of $\overline{Nu}$ reflects the combined effects of the increased area provided by the ribs and the enhanced turbulence by the distortion of velocity and temperature fields caused by existence of the ribs. The mean Nusselt numbers, averaged over one-pitch distance for ribbed channel, are listed in Table 2 for various PR at $Re = 3.3 \times 10^4$. For comparison, $\overline{Nu}_s$ correlated with smooth wall by Dittus and Boelter for the fully developed turbulent channel flow is also listed in

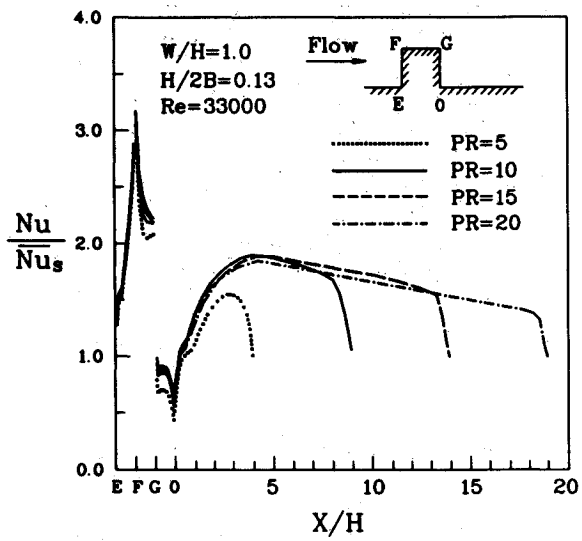

Fig. 11 Streamwise distributions of calculated local Nusselt number for $PR = 5$, 10, 15, and 20 with $H/2B = 0.13$ and $Re = 3.3 \times 10^4$.

Table 2 Area increment and $\overline{Nu}$ enhancement

PR	Area increment	$\overline{Nu}$	$\overline{Nu}$ enhancement
Smooth		82.1	
5	40%	141.2	72.3%
10	20%	159.8	94.0%
15	13.3%	154.6	89.6%
20	10%	145.1	81.0%

Table 2. From Table 2, it is shown that the value of $\overline{Nu}$ for $PR = 10$ is larger than that for $PR = 5$. This is because of the presence of reattachment of the flow for the former case. The reattachment generally is associated with high turbulence intensity and thus enhances heat transfer. For $PR \geq 10$, the $\overline{Nu}$ decreases with increasing PR. The reason is that for $PR \geq 10$ the length of the separation bubble alters slightly as addressed previously, whereas the distance between the reattachment point and successive rib increases with PR, and hence the $\overline{Nu}$ decreases after average over one-pitch distance as PR increases.

Table 2 further shows that owing to the presence of rib pairs the increases in $\overline{Nu}$ for $PR = 5$, 10, 15, and 20 are 72%, 94%, 89%, and 81% of $\overline{Nu}$, respectively, whereas the increases in surface area are 40%, 20%, 13%, and 10%, respectively. Consequently, the increase in $\overline{Nu}$ is much larger than that in surface area due to the presence of rib pairs. The above results are contrary to the calculated results reported by Shakerin et al.[32] in investigating natural convection in an enclosure with discrete roughness elements on a heated vertical wall. This is reasonable because of the lack of heat transfer enhancement by turbulent transport in laminar-flow case.

Summary and Conclusions

The major conclusions of this study are as follows:

1) The current computations with the k-ε-A model which accounts for the anisotropy in turbulence agree relatively well with the measured data and show an improvement over the previous work with the k-ε-E model in the prediction of the turbulent flow and heat transfer characteristics on the rib top and in the separation bubble behind the rib.

2) Incorporating the SCSUDS scheme, the present calculations smoothly and reasonably reproduce the flow details and heat transfer coefficients measured by using LDA and LHI.

3) Both calculated and measured results show the appearance of a major peak of local Nusselt number ratio on the rib top and a second peak located slightly upstream of the reattachment point, whereas the two concave corners formed by the intersection of the rib and channel wall are found to be susceptible to hot spots.

4) The computational results show that enhancement of heat transfer can be accomplished in channel flows using periodic rib pairs and that the increase in heat transfer is more than that in surface area.

5) It is found that increasing the pitch to rib-height ratio causes a decrease in heat transfer augmentation as PR beyond 10. The maximum increase in $\overline{Nu}$ observed in the present study is 94% for $PR = 10$, when a smooth wall of equal projected area is used for comparison.

Acknowledgment

Support for this work was provided by the National Science Council of the Republic of China under Contract NSC 79-04101-E007-01.

References

[1]Webb, R. L., Eckert, E. R. G., and Goldstein, R. J., "Heat Transfer and Friction in Tubes with Repeated-rib Roughness," *International Journal of Heat Mass Transfer*, Vol. 14, No. 4, 1970, pp. 601–617.

[2]Han, J. C., "Heat Transfer and Friction in Channels With Two Opposite Rib-Roughened Wall," *Transactions of the American Society of Mechanical Engineers, Journal of Heat Transfer*, Vol. 106, No. 4, 1984, pp. 774–782.

[3]Han, J. C., Park, J. S., and Lei, C. K., "Heat Transfer Enhancement in Channels with Turbulence Promoters," *Transactions of the American Society of Mechanical Engineers, Journal of Engineering for Gas Turbines and Power*, Vol. 107, No. 3, 1985, pp. 628–635.

[4]Drain, L. E., and Martin, S., "Two Component Velocity Measurements of Turbulent Flow in A Ribbed-Wall Flow Channel," International Conf. on Laser Anemometry-Advances and Application, Manchester, UK, Dec. 1985, pp. 99–112.

[5]Kobayashi, T., Kano, M., and Ishihara, T., "Prediction of Turbulent Flow in Two-Dimensional Channels with Turbulence Promoters," 1st Rept., *Bulletin of the Japan Society of Mechanical Engineers*, Vol. 27, No. 231, 1984, pp. 1893–1898.

[6]Kobayashi, T., Kano, M., Ishihara, T., and Saga, T., "Prediction of Turbulent Flow in Two-Dimensional Channels with Turbulence Promoters," 2nd Rept., *Bulletin of the Japan Society of Mechanical Engineers*, Vol. 28, No. 246, 1985, pp. 2940–2947.

[7]Fodemski, T. R., "The Simulation of Flow and Heat Transfer in Channels with Ribbed Surface," 2nd International Symposium on Transport Phenomena in Turbulent Flows, Tokyo, Japan, Oct. 1987, pp. 867–880.

[8]Pletcher, R. H., "Progress in Turbulent Forced Convection," *Transactions of the American Society of Mechanical Engineers, Journal of Heat Transfer*, Vol. 110, No. 4, 1988, pp. 1129–1144.

[9]Rowley, G. J., and Patankar, S. V., "Analysis of Laminar Flow and Heat Transfer in Tubes with Internal Circumferential Fins," *International Journal of Heat Mass Transfer*, Vol. 27, No. 4, 1984, pp. 553–560.

[10]Rodi, W., *Turbulence Models and their Applications in Hydraulics*, McGraw-Hill, New York, 1984.

[11]Launder, B. E., Reece, G. J., and Rodi, W., "Progress in the Development of a Reynolds Stress Turbulence Closure," *Journal of Fluid Mechanics*, Vol. 68, Pt. 3, 1975, pp. 537–566.

[12]Gibson, M. M., and Launder, B. E., "Ground Effects on Pressure Fluctuations in the Atmospheric Boundary Layer," *Journal of Fluid Mechanics*, Vol. 86, Pt. 3, Mar. 1978, pp. 491–511.

[13]Chen, C. J., *Prediction of Turbulent Flows*, Univ. of Iowa, Iowa City, IA, 1986.

[14]Sultanian, B. K., "Numerical Modeling of Turbulent Swirling Flow Downstream of an Abrupt Pipe Expansion," Ph.D Thesis, Arizona State Univ., Tempe, AZ, 1984.

[15]Launder, B. E., and Spalding, D. B., "The Numerical Computation of Turbulent Flow," *Computer Methods in Applied Mechanics and Engineer*, Vol. 3, No. 2, 1974, pp. 269–289.

[16]Jayatillaka, C. L. V., "The Influence of Prandtl Number and Surface Roughness on the Resistance of the Laminar Sublayer to Momentum and Heat Transfer," *Progress in Heat and Mass Transfer*, Vol. 1, 1969, pp. 193–329.

[17]Leschziner, M. A., "Practical Evaluation of Three Finite Difference Schemes for the Computation of Steady-State Recirculation Flow," *Computer Methods in Applied Mechanics and Engineering*, Vol. 23, No. 3, 1980, pp. 293–312.

[18]Raithby, G. D., "Skew Upstream Difference Schemes for Problems Involving Fluid Flow," *Computer Methods in Applied Mechanics and Engineering*, Vol. 9, No. 2, 1976, pp. 153–164.

[19]Patankar, S. V., *Numerical Heat Transfer and Fluid Flow*, Hemisphere, New York, 1980.

[20]Issa, R. I., "Solution of Implicitly Discretized Fluid Flow Equations by Operator-Splitting," *Journal of Computational Physics*, Vol. 62, No. 1, 1986, pp. 40–65.

[21]Jang, D. S., Jetli, R., and Acharya, S., "Comparison of PISO, SIMPLER, and SIMPLE-C Algorithms for the Treatment of the Pressure-Velocity Coupling in Steady Flow Problem," *Numerical Heat Transfer*, Vol. 10, No. 3, 1986, pp. 209–228.

[22]Liou, T. M., and Kao, C. F., "Symmetric and Asymmetric Flow in a Rectangular Duct with a Pair of Ribs," *Transactions of the American Society of Mechanical Engineers, Journal of Fluids Engineering*, Vol. 110, No. 4, 1988, pp. 373–379.

[23]Sparrow, E. M., and Tao, W. Q., "Symmetric vs Asymmetric Periodic Disturbances at the Walls of a Heated Flow Passage," *International Journal of Heat Mass Transfer*, Vol. 27, No. 4, 1984, pp. 2133–2144.

[24]Chang, Y., "Three-Dimensional Measurements of Turbulent Flows in a Rectangular Duct with Repeated Rectangular-Rib Pairs," M.S. Thesis, National Tsing Hua Univ., Hsinchu, Taiwan, ROC, 1990 (in Chinese).

[25]Hauf, W., and Grigull, U., "Optical Method in Heat Transfer," *Advances in Heat Transfer*, J. P. Hartnett, ed., Academic Press, New York, 1970.

[26]Kline, S. J., and McClintock, F. A., "Describing Uncertainties on Single-Sample Experiments," *Mechanical Engineering*, Vol. 57, Jan. 1953, pp. 3–8.

[27]Hijikata, K., Mori, Y., and Ishiguro, H., "Turbulent Structure and Heat Transfer of Pipe Flow with Cascade Smooth Turbulence Surface Promoters," *Transactions of the Japanese Society of Mechanical Engineers*, Vol. 50, No. 458, 1984, pp. 2555–2562.

[28]Benodekar, R. W., Goddard, A. J. H., Gosman, A. D., and Issa, R. I., "Numerical Prediction of Turbulent Flow Over Surface-Mounted Ribs," *AIAA Journal*, Vol. 23, No. 1, 1985, pp. 359–365.

[29]Amano, R. S., Geol, P., and Chai, J. C., "Turbulence Energy and Diffusion Transport of Third-Moments in a Separating and Reattaching Flow," *AIAA Journal*, Vol. 26, No. 1, 1988, pp. 273–282.

[30]Driver, D. M., and Seegmiller, H. L., "Features of a Reattaching Turbulent Shear Layer in Divergent Channel Flow," *AIAA Journal*, Vol. 23, No. 4, 1985, pp. 163–171.

[31]Chen, C. J., and Yoon, Y. H., "Finite Analytic Numerical Solution Axisymmetric Navier-Stokes and Energy Equations," *Transactions of the American Society of Mechanical Engineers, Journal of Heat Transfer*, Vol. 105, No. 3, 1983, pp. 639–645.

[32]Shakerin, S., Bohn, M., and Loehrke, R. I., "Natural Convection in an Enclosure with Discrete Roughness Elements on a Vertical Heated Wall," *International Journal of Heat Mass Transfer*, Vol. 31, No. 7, 1988, pp. 1423–1430.